Chapter 3

Dynamic magnetic responses in ensemble of anisotropic two-dimensional nanosystem decorated over nanoparticles

3.1 INTRODUCTION

The ensemble of interacting magnetic nanoparticles has irresistibly unique dynamic magnetic behaviour arising from the strength and type of interactions among primary nanosystems [1-3]. With variation in the degree of interaction strength among primary constituents, the magnetic behaviour can be controlled in the ensemble [4-6]. The interaction can be controlled with various parameters including organization geometry of the ensemble, spatial arrangement of primary nanoparticles, interparticle spacing, etc. [7-10]. However, size/shape of MNPs can modulate the collective magnetic behaviour of the ensemble owing to modification in their magnetic anisotropy energy [10-13]. Hence, an in-depth spin dynamics study is crucial to fully comprehend the dynamic magnetic responses of such an ensemble.

Among various anisotropic morphology of primary nanosystems, the ensemble of anisotropic two-dimensional (2D) primary nanoflakes is intriguing to achieve rationally modified magnetic behaviour than that of the other morphological counterparts [14, 15]. Anisotropic two-dimensional geometry of primary nanosystems confers extraordinary behaviour because of modulation in shape anisotropy, magnetic anisotropy energy, etc. [16-21]. The dominance of interaction among the primary anisotropic nanosystems can show fascinating slower spin dynamics with the evolution of low-temperature magnetic frustrated states [21, 22]. The interfacial spin arrangement and the type of interaction (either

This part of thesis is Communicated as "K. Konwar, et al. Non-ergodic quantum phenomena in cluster spin glass ensemble of two-dimensional nanoflakes and a dis-integrated framework."

dipolar or exchange interaction) among the primary 2D flakes in such anisotropic nanosystems lead to complexity in the anisotropy energy landscape [23]. In addition, an interplay between dipole and exchange interaction can further control the thermodynamic non-equilibrium spin dynamics at low temperature with non-ergodic quantum phenomena. Hence, the geometrical pattern of the ensemble can be considered to describe diverse types of dynamic magnetic responses.

This chapter provides detailed spin dynamics represented by considering the structural topology of an ensemble of two-dimensional Manganese dioxide flakes decorated over nickel ferrite nanoparticles, δ-MnO_2@$NiFe_2O_4$, referred to an Ensemble of Two-Dimensional (2D) flakes (ETD). With the aid of *ab initio* based DFT calculations, ground-state magnetic analysis is investigated in the respective constituent geometry. The relation between spin frustration with non-equilibrium dynamics is drawn by considering anisotropic morphology. The dynamic magnetic responses are drawn by dc and ac susceptibility and out-of-equilibrium characterizations. The structural property correlation is understood following SAXS and SANS. The strong interaction among the constituent systems results deeper in metastable states valley, with the evolution of Cluster SG state. A fascinating dynamic behaviour with significant anisotropy field, enhanced magneto-crystalline anisotropy, robust bonding between δ-MnO_2 and $NiFe_2O_4$, and prominent MME with substantial ageing relaxation is represented herein.

3.2 EXPERIMENTAL DETAILS

The considered system is developed using two-step synthesis procedure [24] and the required precursors are achieved from Zenith India. $NiFe_2O_4$ nanoparticles is developed via a hydrothermal procedure. An appropriate stoichiometric amount of $FeCl_3.6H_{20}$, $NiCl_2.6H_2O$, urea, and Polyvinylpyrrolidone (PVP) is considered to dissolve in DI-water to achieve a homogenous solution. The homogeneous solution is autoclaved in a Teflon-lined autoclave at 180°C for 12 h in a hot air

oven. The solution in the autoclave is kept for cooling up to 300 K. The precipitate is collected by following centrifugation and washed multiple times considering water and ethanol alternately. The sample is collected after drying the precipitate for 12 h at a temperature of 80°C. After obtaining Nickel Ferrite ($NiFe_2O_4$) nanoparticles, the decoration of Manganese dioxide (δ-MnO_2) over $NiFe_2O_4$ nanoparticles is accomplished following a modified hydrothermal procedure [24]. A stoichiometric amount of Potassium Permanganate ($KMnO_4$) is dissolved in an appropriate amount of DI water to get a homogeneous solution. 1.4 mL of 37 wt% hydrochloric acid (HCl) is added to this homogeneous solution dropwise during mechanical stirring. After a few minutes, an amount of 0.4 g of $NiFe_2O_4$ is added and kept for sonication for 15 mins to get a well-dispersed solution. The entire solution is transferred to an autoclave at 110°C for 6 h to get the phase δ-MnO_2. The hydrothermal reaction for 6 h is performed to achieve an ensemble of 2D Manganese Oxide flakes decorated over nickel ferrite nanoparticles. The solutions are allowed to cool down naturally and the precipitations are obtained by centrifugation and multiple time washing following water and ethanol. The final precipitations are dried at 60°C for 12 h. Field Emission Scanning Electron Microscopy (FESEM) is performed in a model ZEISS, SIGMA with an acceleration voltage 0.5-30 kV. X-ray photoelectron spectroscopy (XPS) is performed in an X-ray photo spectrometer with Al K_α source and hυ of 1486.6 eV. The JSM 6390LV model is used for energy-dispersive X-ray (EDX) analysis. The rest of the instrumental details are the same as mentioned in chapter 2.

3.3 COMPUTATIONAL DETAILS

The *ab initio* Density functional theory (DFT) simulations are employed to simulate the electronic property of δ-MnO_2@$NiFe_2O_4$ as shown in Figure 3.2(a). The ferromagnetic ground state has been achieved self-consistently by considering the effect of spin-polarization. The spin-polarized calculations were based on the Kohn-Sham equation with plane-wave basis sets as incorporated in the Quantum ESPRESSO software package [25]. The considered system, δ-

MnO_2@$NiFe_2O_4$ as shown in Figure 3.2(a), has 92 atoms to fulfil the *ab initio* calculations for various tenacities such as electronic properties, magnetic moment calculations, and spin-density distributions. The optimized crystal geometry is performed using the Broyden-Fletcher-Goldfarb-Shanno (BFGS) algorithm. The system exhibits 852 electrons and 511 KS states. The electron-core corrections are executed by ultrasoft pseudopotentials (USPP) formed by Rappe-Rabe-Kaxiras-Joannopoulus (RRKJ) method [26]. The exchange correlation term is approximated via local density approximation (LDA) [27] and the strongly-correlated interaction is taken into consideration in such an oxide-based systems by incorporating the exchange parameters (Hubbard, U ~ 4 eV) [28]. The Brillouin zone (BZ) sampling is supported by contemplating a 3 x 3 x 3 unshifted Monkhorst-pack (MP) grid [29] for achieving the convergence of the system. The cut-off energy,40 Ry, is preferred for expanding plane-wave basis sets considering 10^{-6} Ry convergence threshold following Davidson diagonalization. The electronic structure calculation is performed considering a denser k-mesh grid 9 x 9 x 9 through the tetrahedron method non-self-consistently. The high-symmetric k-path Γ-X-M-Γ has been considered for electronic band structure calculation.

3.4 RESULTS AND DISCUSSIONS

3.4.1 Microstructural study

The Core-level XPS study is performed as shown in Figure 3.1(a-d) for surface analysis to attain to ensure the elemental compositions and electronic state analysis. As shown in Figure 3.1(a), the main peaks of Mn 2P peaks are observed at around 642.30 eV and 654.10 eV corresponding to Mn $2P_{1/2}$ and Mn $2P_{3/2}$ with an energy separation of 11.80 eV, validating the presence of δ-MnO_2 [30, 31]. Further, Figure 3.1(b) shows the main peaks of Ni 2P at around 872.0 eV and 854.90 eV corresponding to Ni $2P_{1/2}$ and Ni $2P_{3/2}$ with an energy separation of

17.10 eV [30]. Two shake-up satellite peaks are observed at around 861.40 eV and 880.10 eV confirming the existence of Ni^{2+} [31].

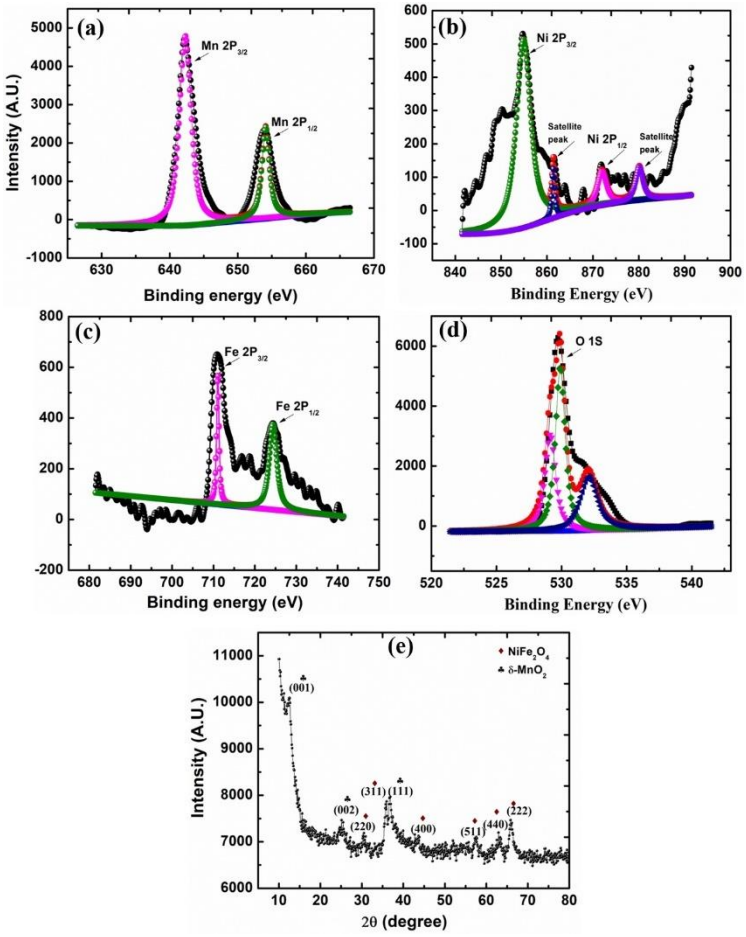

Figure 3.1: Microstructural study: Core-level X-ray photoelectron spectroscopy (XPS) study (a) Mn 2P, (b) Ni 2P, (c) Fe 2P, (d) O 1s; and (e) X-Ray Diffraction (XRD) pattern of Ensemble of Two-Dimensional flakes (ETD).

The detailed Fe 2P spectrum is shown in Figure 3.1(c), which represents peaks at around 711.0 eV and 724.0 eV for Fe $2P_{1/2}$ and Fe $2P_{3/2}$ [32, 33]. Three distinct peaks are observed for the O 1S spectrum at around 529.1 eV, 529.9 eV, and 532.1 eV respectively [30-33] as shown in Figure 3.1(d). The peak observed at 529.1 eV is arising from the typical metal-oxide (Metals: Fe, Ni, Mn) bond. The peak at 529.9 eV is due to defect sites along with the peak at around 532.10 eV, which can be related to physically/chemically absorbed surface moisture. The electronic

state analysis ensures the formation of δ-MnO_2@$NiFe_2O_4$. Further, X-ray diffraction (XRD) of as-synthesised system is performed to confirm the crystal phase as shown in Figure 3.1(e). The planes are observed at around (001), (002), and (111) corresponding to the formation of δ-MnO_2 (JCPDS file number 80-1098). Further, the observed planes (220), (311), (400), (511), (440), and (222) confirm formation of cubic spinel phase of $NiFe_2O_4$ (JCPDS Card No. 10-0325) [24] having space group Fd-3m. Hence the formation of δ-MnO_2@$NiFe_2O_4$ is confirmed with dominance of cubic phase.

For morphological study, FESEM study is performed, which shows fascinating flower-like hierarchical assemblies for system δ-MnO_2@$NiFe_2O_4$ as shown in Figure 3.2(a, b). The thickness of 2D flakes is roughly around 3-4 nm and curvy shaped flakes are also observed. The 2D flakes are decorated over Nickel Ferrite nanoparticles. Additionally, TEM images are given in Figure 3.2(c, d). The secondary structure has a diameter of nearly 300 nm with flakes of diameter 20-40 nm. For further structural correlation investigation, SAXS and SANS are employed as shown in Figure 3.2(e). SAXS provides the details about the primary nanosystems and SANS gives the insight of secondary structure correlation [34, 35]. SAXS intensity profile is fitted by considering the form factor of the homogeneousXS model of the planar object. The form factor in case of an anisotropic system having local planar geometry can be represented as multiplicative term comprised of a cross section form factor term represented as $P_{cs}(q)$ related for shorter dimensions and a shape factor named $P'(q)$ related to larger dimensions, and can be represented as [44]: $P_{planar}(q) = P_{cs}(q)\,P'(q)$. $P_{cs}(q)$ is dependent on the structural parameters related to the inner structure of the layer having short dimensions, whereas the shape form factor $P'(q)$ explains the entire shape in terms of larger dimensions with some polydispersity [34, 35]. The cross-section form factor $P_{cs}(q)$ for homogenousXS model can be represented as:

$$P_{cs}\,(q, \eta, L) = \left(\eta L\ \frac{\sin(\frac{qL}{2})}{\frac{qL}{2}}\right)^2 \tag{3.1}$$

where L gives the detail about the thickness of the planar object, η represents the scattering constant, and q gives the scattering vector. After proper fitting, achieved parameters ensure the presence of a planar object as a primary constituent with thickness (L) of 2.25 nm and diameter, 55 nm.

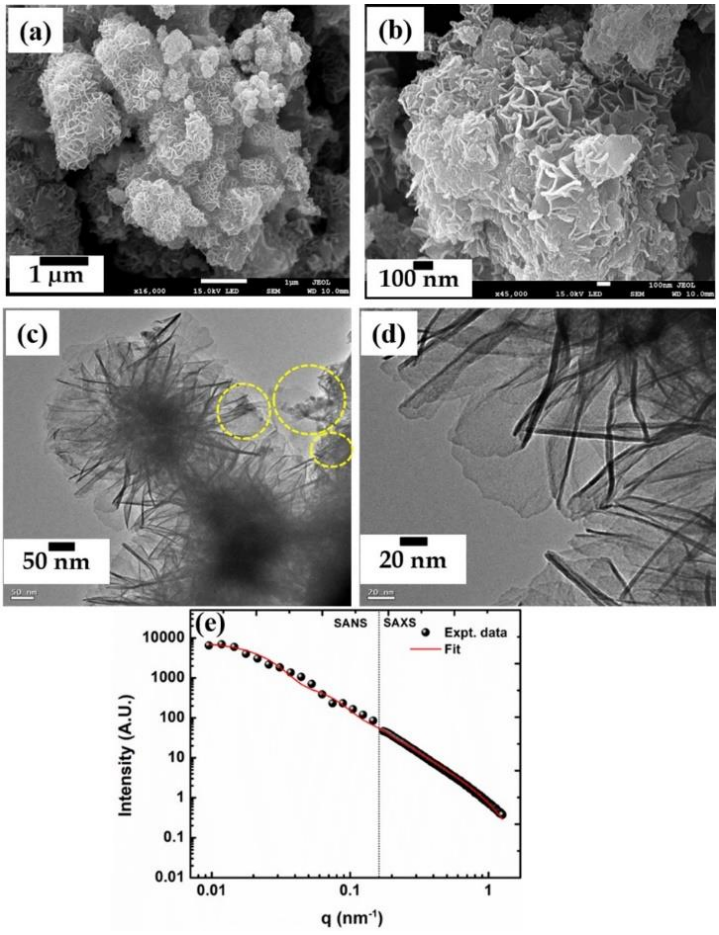

Figure 3.2: Microstructural study: (a, b) FESEM (c, d) TEM images, (e) SAXS-SANS intensity profile fitting of Ensemble of Two-Dimensional flakes (ETD) (The distribution of Nickel Ferrite nanoparticles is shown in yellow circle in Figure (c)).

Another spherical model form factor is considered with log-normal size distribution [34]:

$$F(q,R) = 3\frac{\sin(qR)-qR\cos(qR)}{(qR)^3} \quad (3.2)$$

The presence of spherical nanoparticles of radius, R, of 15 nm size with a polydispersity of 0.40 is considered with log-normal size distribution. The planar form factor is the contribution from 2D flakes of MnO_2 and the spherical form factor is a contribution from Nickel Ferrite nanoparticles. Further, the SANS intensity profile is fitted using spherical form factor having a 150 nm radius and 0.35 polydispersity inde. The SANS profile fitting gives an idea of structural parameters of hierarchical assemblies. The SAXS-SANS studies clearly show that there are two types of hierarchical patterns in the systems.

Table 3.1 Elementary composition achieved from EDX analysis.

Element	Weight %	Atomic %
Mn	53.68	30.18
Ni	4.01	2.11
Fe	10.15	5.61
O	32.17	62.10

The elementary mapping for the constituent elements is further represented following EDX analysis as shown in Figure 3.3 confirming the presence of Mn, O, Ni, and O with elementary composition as shown in Table 3.1. The intense peak in the low energy range in the sum spectrum is due to Carbon tape. Moreover, it is reflected from the EDAX colour mapping that the elements are distributed uniformly and present everywhere, which is due to capturing a large-scaled micrograph (in μm).

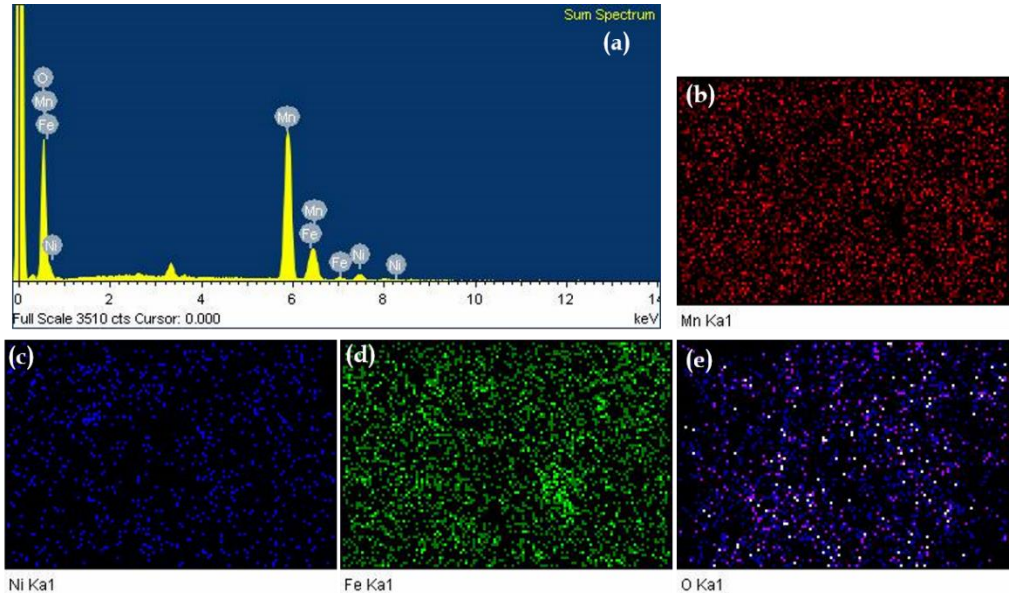

Figure 3.3: EDX microanalysis of Ensemble of Two-Dimensional flakes (ETD): (a) Sum spectrum of all the elements, (b) elementary mapping of Mn, (c) elementary mapping of Ni, (c) elementary mapping of Fe, (d) elementary mapping of O.

3.4.2 Atomic Configuration and Electronic structure

Figure 3.4 (a) shows the crystal geometry of constituent δ-MnO_2@$NiFe_2O_4$. The lattice parameter is found to be 8.48 Å. The ground state ferromagnetic structure is achieved self-consistently with a total magnetization of 57.68 μ_B/cell for δ-MnO_2@$NiFe_2O_4$. The total Kinetic energy is found to be -9308.3 Ry. The robust bonding between $NiFe_2O_4$ and two-dimensional architecture (δ-phase) of MnO_2 is expected from the obtained kinetic energy. This is also evident from band structure (as shown in Figure 3.4(b)), as δ-MnO_2@$NiFe_2O_4$ depicts sharp features of the band structure. Figure 3.4(b) represents the spin-resolved electronic structure of δ-MnO_2@$NiFe_2O_4$. The system exhibits a metallic nature at the Fermi energy (E_F) region [36]. The sharp spike-like features in the density of states (DOS) pattern (as shown in Figure 3.4(c)) signifies the presence of ferromagnetic behaviour [36, 37]. The ferromagnetic ordering remains unaffected after incorporating $NiFe_2O_4$ with δ-MnO_2, instead variation in total magnetization value is observed.

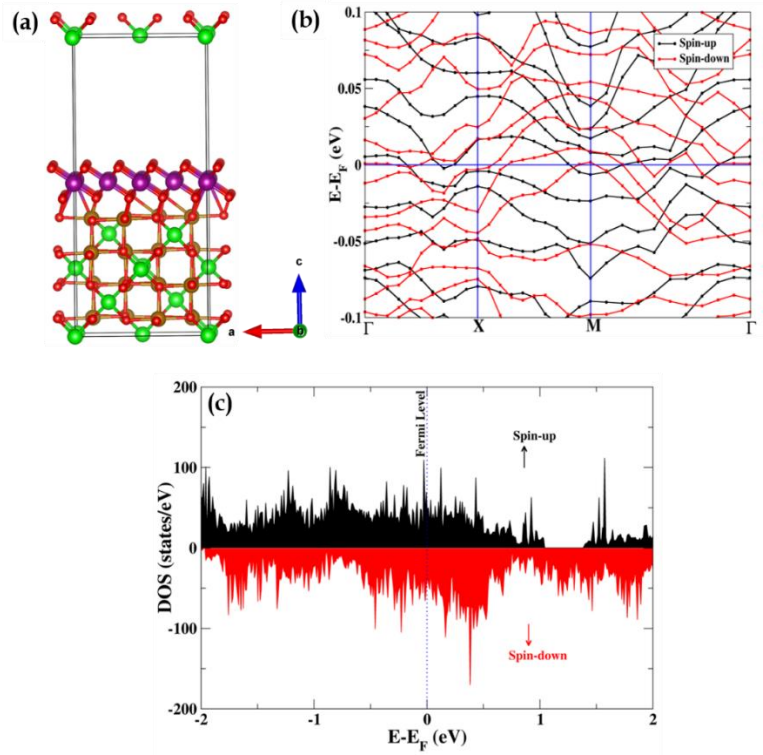

Figure 3.4: (a) Atomic configuration: the violet colour for manganese (Mn), green colour for nickel (Ni), golden colour for iron (Fe), and red spheres oxygen (O), (b) Electronic band structure, and (c) determination of density of states (DOS) of Ensemble of Two-Dimensional flakes (ETD).

Figure 3.5(d) depicts spin density distribution of the system ETD with an iso-surface value of 0.0529096 e/Å^3. The yellow and blue cyan colours depict parallel and antiparallel states, respectively. The average magnetic moment per Mn atom site in δ-MnO_2@$NiFe_2O_4$ is found to be 0.17 μ_B depicting the parallel states (yellow colour) in Mn site, which signifies the robust interaction with $NiFe_2O_4$ system. Figure 3(b) depicts the electron density distribution mapping of δ-MnO_2@$NiFe_2O_4$ in intensity range from 0 to 1, where red and cyan colours depict electron localization and delocalization of the structures, respectively. This correlates well with the Figures 3(a) and (c). Figure 3(c) displays the projected density of states (PDOS), which defines orbital contribution of the system ETD. Figure 3(c) displays the PDOS where the orbital contribution of Fe, Mn, Ni, and O atoms in both the left and right panels follows the same trend. Electronic

structure calculation of δ-MnO_2@$NiFe_2O_4$ exhibits both parallel and antiparallel states. Such interpretation provides a hint about the occurrence of exchange interaction in the system ETD [36-38]. The trend of PDOS (Figure 3(c)) corroborates well with the spin density distribution as shown in Figure 3(a).

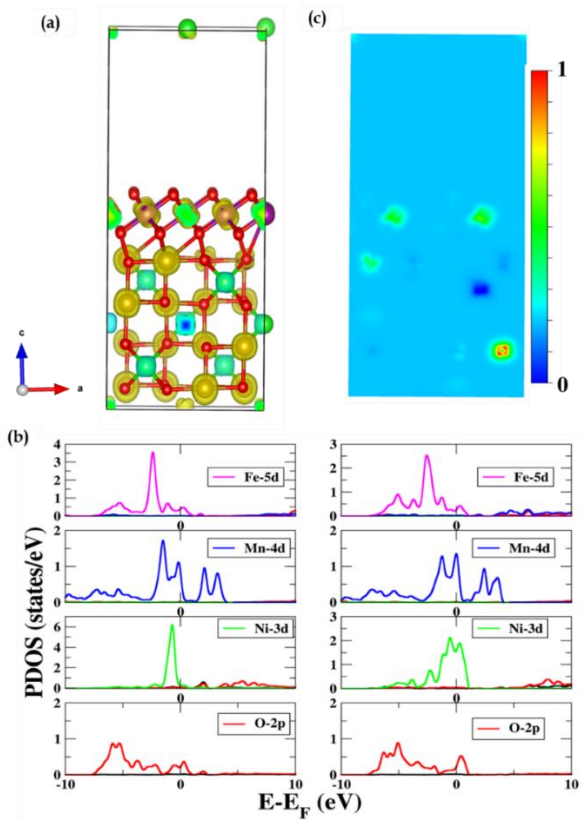

Figure 3.5: (a) Spin density distribution with an iso-surface value of 0.0529096 e/Å^3, (b) Projected density of states (PDOS) individually for iron (Fe), manganese (Mn), nickel (Ni) and oxygen (O), respectively. (c) Electron density distribution with an intensity range of 0 to 1 of Ensemble of Two-Dimensional flakes (ETD).

3.4.3 Direct Current Magnetization study

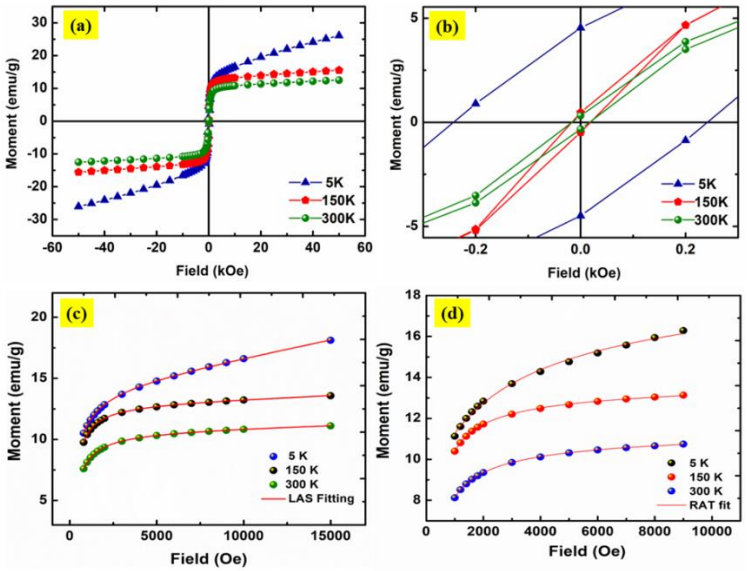

Figure 3.6: DC magnetization of Ensemble of Two-Dimensional flakes (ETD).: (a) Field-relying magnetization, (b) Zoomed view of hysteresis loop at different temperatures, (c) LAS fitting at 5 K, 150 K, and 300 K, (d) Random Anisotropy Theory (RAT) fitting at 5 K, 150 K, and 300 K.

The field-relying magnetization study is shown in Figure 3.6(a, b, c, d) at 300 K, 150 K, and 5 K respectively for system ETD. The 'S' shaped hysteresis pattern shows possibility of superparamagnetic phase at room temperature [35]. The coercivity (H_c) and remanence (H_r) values are calculated, [$H_c = (H_c^+ + H_c^-)/2$ and $H_r = (H_r^+ + H_r^-)/2$] as H_c = 17.0 Oe and H_r = 0.310 emu/g for 300 K, H_c = 17.70 Oe and H_r = 0.480 emu/g at 150 K, H_c = 242.0 Oe and H_r = 4.50 emu/g at 5 K respectively. The low-temperature ferromagnetism is the signature of such superparamagnetic systems. For magneto-crystalline anisotropy constant and saturation magnetization measurements, law of approach to saturation (LAS) model [39] is considered.

The LAS fitting is performed for a range of 500 Oe to 15000 Oe with varied temperatures to observe the thermal-dependent magneto-crystalline anisotropy as shown in Figure 3.6(c). However, magnetization dependency on applied field

is generally explained by considering LAS as mentioned in equation 2.7 of Chapter 2. The LAS fitting is considered at 5 K, 150 K, and 300 K as shown in Figure 3.6(c). After proper fitting, saturation magnetization, M_s = 14 emu/g and cubic anisotropy constant K = 1.3 × 10^4 erg/cm^3 is found at 5 K; at 150 K: M_s = 12.9 emu/g and K = 4.2 × 10^3 erg/cm^3; at 300 K: M_s = 10.7 emu/g and K = 8.1 × 10^3 erg/cm^3. A sufficiently high anisotropy is evident from the LAS investigation at low temperature.

Moreover, Random Anisotropy Theory (RAT) [40] is considered to evaluate role of magnetic anisotropy in regime of low temperature by fitting the field relying on magnetizations as shown in Figure 3.6(d). In accordance with this theory, strength of random anisotropy field may be used to forecast the magnetic ground state, which results in prediction of multiple magnetic ground states. The H strength is evaluated by H_s using the expression [40]:

$$H_s = {H_r^4}/{H_{ex}^3} \tag{3.3}$$

where H_r and H_{ex} represent the anisotropic field and exchange field. If H < H_s then there exists a correlated spin-glassy phase in the system with large susceptibility like Ahrony and Pyte phase. The random anisotropy can change the locally coupled regime's magnetization direction and magnetization is represented here as [40]:

$$M = M_0[1 - \frac{1}{15}\left(\frac{H_s}{H}\right)^{\frac{1}{2}}] \tag{3.4}$$

where M_0 stands for saturation magnetization. When the applied field becomes too high, spins tend to a virtual alignment along the applied external field and have a tiny tipping angle as a result of anisotropy. If induced magnetic energy surpasses the energy related to the exchange field, the field response magnetization curve starts to saturate and magnetization is represented as [40]:

$$M = M_0\,[1 - {1}/{15}\,(H_r/H + H_{ex})^2] \tag{3.5}$$

After fitting with M-H data for the range of 1000 Oe to 9000 Oe at 5 K, the fitting parameters are evaluated as H_r = 6075 Oe and H_{ex} = 2150 Oe at 5 K. Such a higher value of H_r is the signature of glassy magnetic systems, where freezing of correlated spins leads to the high strength of anisotropy field at low temperature. Hence, the temperature-dependent magnetization trend is imprinted to understand the trend of blocking/freeing of constituent moments.

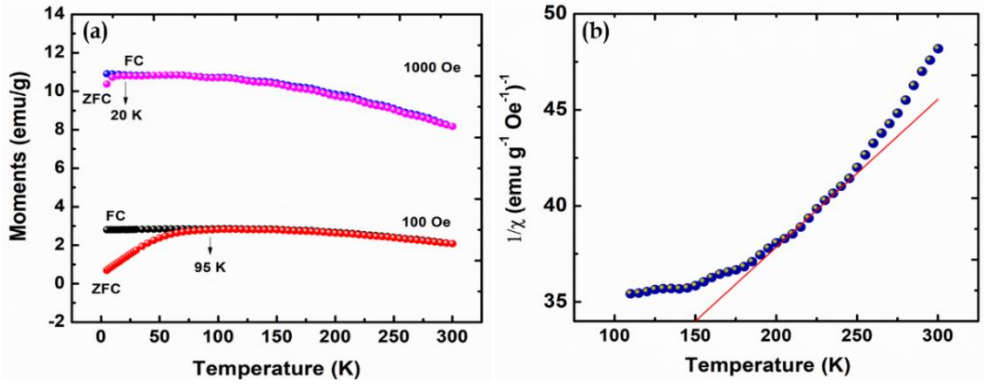

Figure 3.7: (a) Temperature-dependent magnetization study of Ensemble of Two-Dimensional flakes (ETD) at field 1000 Oe and 100 Oe (Blocking temperature is shown with a downward arrow in both the ZFC curve); (b) CW law fitting and the red fitting line represents CW law fitting line.

The ZFC and FC conditions are taken for execution of temperature-dependent irreversible magnetization measurement between 2 K and 300 K at magnetic fields 100 Oe and 1000 Oe as shown in Figure 3.7(a). The divergence between the ZFC-FC magnetization (known as bifurcation) is observed far below the room temperature at all the magnetic field conditions, which ensures the possible existence of a spin-glass-like nature or interacting superparamagnetic phase in the system [35]. However, the non-zero M_{irr} defines existence of SG transition temperature at a working magnetic field and particular characteristic measuring period [41]. The competition among the spins in the interface of $NiFe_2O_4$ and MnO_2 is likely to evolve magnetic frustration in the structure. However, the combined effect of nearest-neighbor interaction along with spin frustration is liable for the development of SG. FC curve exhibits a pronounced cusp at

temperature around ~ 95 K and ~ 20 K at fields 100 Oe and 1000 Oe respectively. Magnetization is slightly decreasing with a decrease in temperature below the cusp, supporting the existence of interaction among individual entities and possibilities of new magnetic states such as the glassy magnetic states. Moreover, the trend of $\Delta\chi$ (difference between ZFC and FC moments) with applied field shows expected formation of a spin-glass state or interacting superparamagnetic state. $\Delta\chi$ shows a lowering value with an increase in field at a low-temperature region, which is a typical signature of interacting spins [72]. Such behaviors are generally a signature of a frozen SG state or interacting superparamagnetic phase [41]. Hence ac susceptibility and out-of-equilibrium experiments are performed.

Additionally, as shown in Figure 3.7(b), the inverse susceptibility, $1/\chi$, is performed in the high-temperature region, T> 100 K, and the data is fitted with modified CW law [42]:

$$\chi = \chi_0 + \frac{C}{T-\theta_{CW}} \tag{3.6}$$

Herein, χ_0 is the thermal energy independent susceptibility, which is a summation of susceptibility for diamagnetic Larmor core, Landau susceptibility, and Pauli paramagnetic spin related to conduction electrons [41]. C is the Curie constant and CW temperature is written as θ_{CW}. θ_{CW} = 150 K with Curie constant, C = 13 $cm^3K\ mol^{-1}$ is found. From the Curie constant, effective magnetic moment of the system is found as $\mu_{eff} \sim 10\mu_B$. The dominant ferromagnetic interaction is ensured by positive CW temperature and in accordance with mean-field theory, θ_{CW} is the sum of entire exchange couplings of the spins. An in-depth understanding of such interacting SG system/interacting superparamagnetic system and the role of anisotropy are further explored by an ac susceptibility study as provided in the next section.

3.4.4 AC susceptibility study

AC susceptibility is employed to inspect spin dynamics by considering frequency in the range of 93 Hz to 9724 Hz and temperature in 2-350 K range. The impact against perturbation imposed by the exciting 10 Oe ac field is recorded. The frequency dependence of real (χ') and imaginary (χ'') components of ac susceptibility is presented in Figure 3.8(a, b) as a function of temperature.

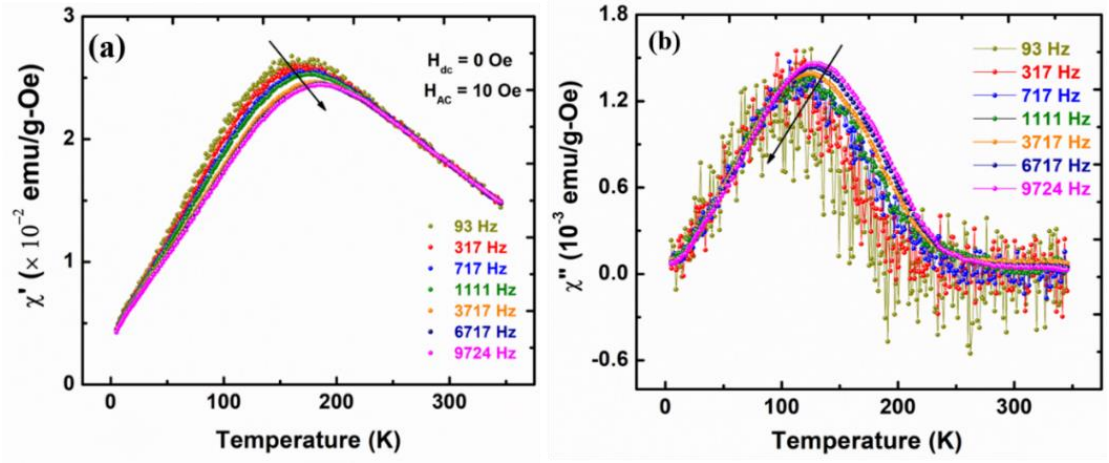

Figure 3.8: AC susceptibility (a) in-phase, (b) out-of-phase of Ensemble of Two-Dimensional flakes (ETD)**.** The arrow mark indicates the change in T_{max} and χ_{max} with an increase in frequency.

At 93 Hz, a distinct anomaly is found at around 160 K, which endorses a frequency-dependent trend. As shown in Figure 3.8(a), frequency-dependent curves demonstrate that peak location shifts towards a higher value of temperature as a result of an extension of action time-induced delay of spin relaxation and peak height lower as the frequency of excitation wave increases [41]. The observed frequency-dependent behaviour is a hallmark of either the presence of spin-glassy freezing or superparamagnetic blocking. To ensure the underlying condition for such peak shifting, the Mydosh parameter, k, is considered to be calculated using equation 2.9 of Chapter 2. After calculating, the k value is found as ~ 0.09. In case of a superparamagnetic system where there is no interaction among the nanoparticles, k gives a value between 0.1 to 0.28. k

shows a value of an order of 10^{-2} – 10^{-3} in the case of an interacting system or system having a spin-glass phase. The obtained values are higher than those of canonical spin-glass systems. But, such a value of k in the range of 0.01 to 0.09 is sometimes in cluster spin glass systems and interacting superparamagnetic systems [41]. Hence, further analysis of spin dynamics is needed to ensure whether the systems reside in the category of cluster spin-glass or interacting superparamagnetic. The trend of $\chi'(T)$ is attributed to the freezing of interacting spin clusters that are oriented randomly below freezing temperature or blocking of spins below the superparamagnetic state. In addition, the Mydosh parameter mimics the sensitivity to frequency, which is highly dependent on interactions among underlying elements [41, 43]. As magnetic clusters are weakly interacting, sensitivity is stronger. As opposed to that, in highly interacting magnetic systems, high frequency is needed to detect the substantial shift in ac susceptibility.

For further analysis, frequency-relying freezing temperature is described considering Vogel-Fulcher (VF) model fitting and standard critical slowing down power law. Before that, Arrhenius law is employed, similarly as mentioned in Chapter 2, equation 2.10, to fit the frequency-dependent freezing temperatures/blocking temperatures. The linear fit as shown in Figure 3.9(a) results in spin flipping period, τ_0 and activation energy, $\frac{E_a}{k_B}$ as 1.10×10^{-15} s and 4447.90 K. But $\frac{E_a}{k_B}$ gives an unphysical high value and τ_0 gives an unphysical slower relaxation of single spin flip [41]. Such unphysical results lend more credence to the claim that spin dynamics are not just the result of single spin flips but instead have a collective behaviour owing to interactions across clusters. Hence, the dynamical scaling Vogel-Fulcher (VF) law is utilised for spin freezing dynamics of interacting spins as per equation 2.11 of Chapter 2.

As shown by the fitting in Figure 3.9(b), the best fitting with the VF equation leads to the values of the spin flipping period, τ_0 , VF temperature, T_0 and

activation energy, $\frac{E_a}{k_B}$ as τ_0 = 1.90 × 10^{-8} s, T_0 = 111.20 K, and $\frac{E_a}{k_B}$ = 545.0 K. The non-zero values of VF temperature (T_0) with physical parameters support VF law's applicability and suggest the development of clusters due to the interaction among spins. The obtained value of τ_0 is shorter than the typical atomic spin flipping, that is nearly in 10^{-13} s order. The observed spin relaxation period lies in luster SG range. The activation energy is showing a trend of $\frac{E_a}{k_B}$ ~ 4.9 T_0, where T_0 is the strength of coupling among magnetic spin clusters. If $\frac{E_a}{k_B}$ >> T_0, the magnetic clusters are expected to couple weakly. Herein the system shows interacting coupling which resides in the intermediate range, hinting existence of finite interactions among the spin clusters. In addition, by considering the Tholence criterion, $\delta T_{Th} = \frac{T_f - T_0}{T_f}$, a value of 0.17 is found, further validating the presence of cluster SG [41-43].

For further clarification of phase transition, dynamic scaling theory is employed. In accordance with dynamic scaling theory, we consider the power law, which is a primary law to examine the frequency-dependent freezing temperature. The frequency-dependent T_f is fitted using power law following the dynamic scaling model [41] as provided in Chapter 2, equation 2.12. The fitting is shown in Figure 3.9(c) as log(τ) vs T_f and the best fittings are found as relaxation period, τ* = 6.3 × 10^{-8} s, critical exponent, zv' = 6.2, and glass transition temperature, T_g = 151.6 K. The obtained physical values provide insight into spin dynamics. The observed values of τ* and zv' further confirm that δ-MnO_2@$NiFe_2O_4$ belongs to the family of cluster SG systems, which has a typical range of τ* between 10^{-7} to 10^{-11} s and zv' has a range between 4 to 12 [41-43].

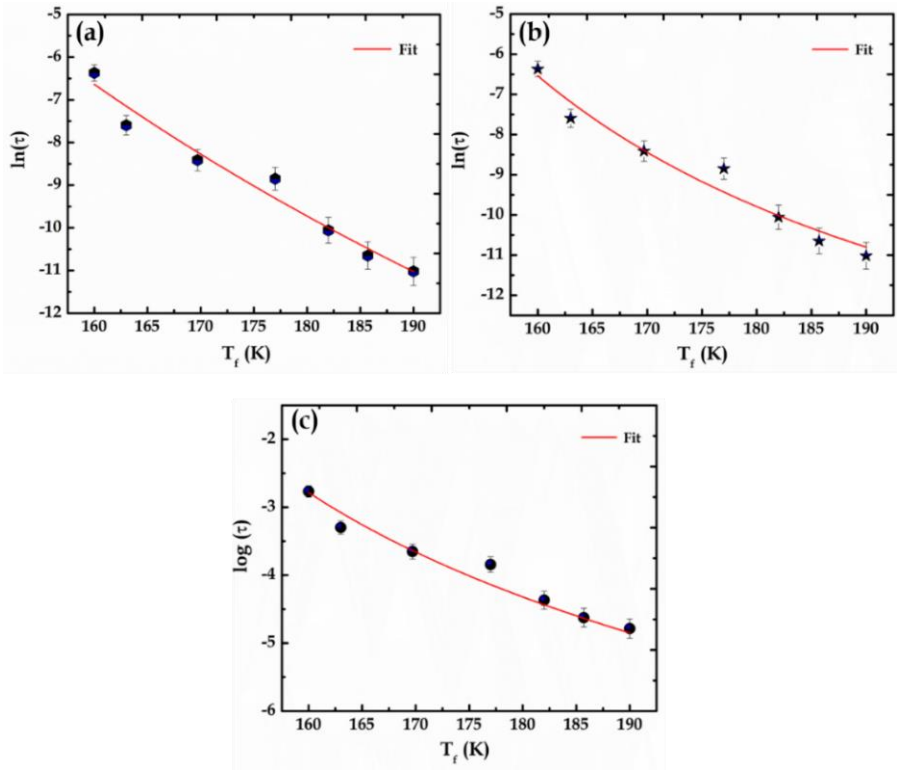

Figure 3.9: (a) Arrhenius equation fitting, (b) VF-fitting, (c) Critical slowing down model fitting of Ensemble of Two-Dimensional flakes (ETD). The error bars in represent standard deviation in experimental data.

3.4.5 Nonequilibrium dynamics

3.4.5.1 Magnetic memory effect

Thermal history-dependent magnetization measurements are complementary signatures of Spin Glass phenomena in frustrated spin systems [41-44]. Generally, during the measurement of magnetic moment as a function of time, the moment is observed slow decrease/increase with applied field, which proposes spin relaxation towards a stable equilibrium state of spin landscape [44]. To confirm the existence of nonergodicity, a magnetic memory

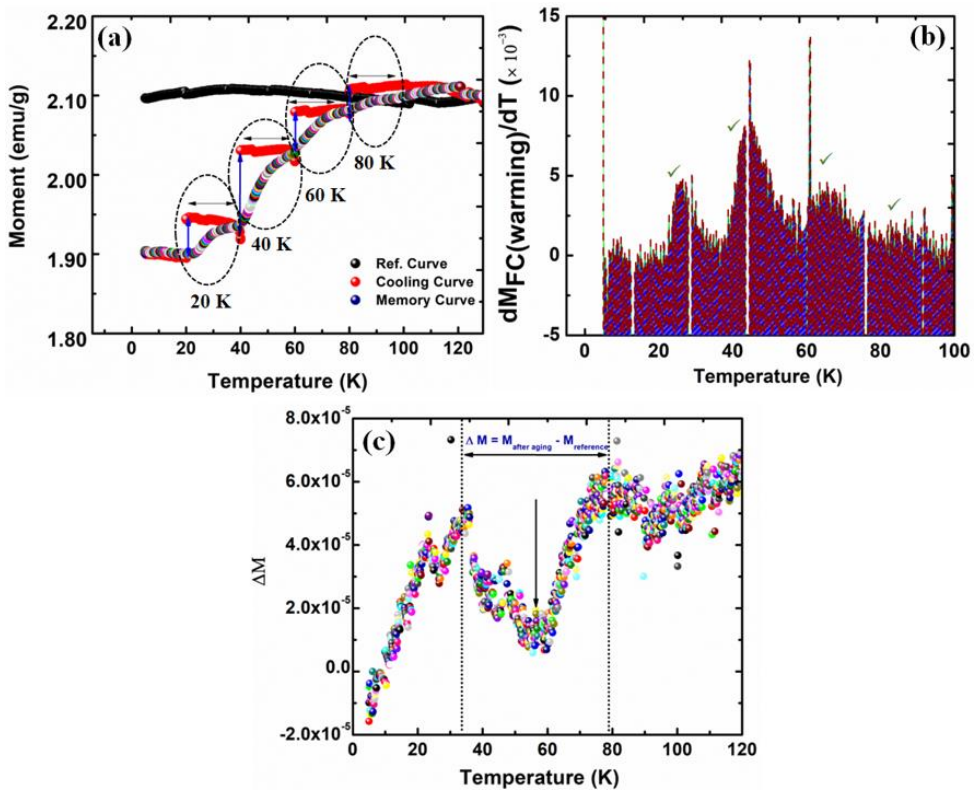

Figure 3.10: (a) FC magnetic memory effect, (b) Differentiation of FC magnetic memory effect, (c) ZFC magnetic memory effect of Ensemble of Two-Dimensional flakes (ETD).

effect study is executed considering FC-ZFC protocols. For FC cooling, the cooling of systems is imposed from room temperature to 5 K in the presence of a 50 Oe dc field of following some intermediate stoppage. Four different stopping temperatures, T_{stop}, such as 20.0 K, 40.0 K, 60.0 K, and 80.0 K are considered below glass freezing/blocking temperature and the field is turned off for 1 h at individual stopping temperature for relaxation. A step-like behaviour during this stage is obtained and the curve is named as "cooling" as shown in Figure 3.10(a). Once the lowest stabilized temperature is reached, the temperature is raised to 300 K in presence of field without any stoppage and moment is recorded to obtain the warming curve named as 'Memory curve'. A discernible uptrend of moment is observed near each stopping temperature such as 20 K, 40 K, 60 K, and 80 K, ensuring the existence of thermal memory and confirming that the systems can

memorise its past thermal history. The reference curve is measured without any intermediate interruption at the same applied magnetic field. To confirm the thermal memory history in more detail, differentiation of memory curve is performed with respect to temperature as shown in Figure 3.10(b) and memory of each halt temperature is confirmed.

Similarly, the Zero Field Cooling (ZFC) magnetic memory effect [44, 45] is also studied to check whether the system can remember its thermal history at zero field cooling condition or not [45, 46]. For that, system is cooled down to 40 K, far below freezing temperature, at zero magnetic field and held for a duration of 1 h. After completing the wait period, further cooling of the system is performed till 2 K. At this certain point, warming is executed in 100 Oe field and the moments, $M_{mem, ZFC}$, are recorded. Reference is recorded by considering the ZFC protocol without any intermediate perturbation. The reference curve with memory curves is showing overlapping at the region of interruption. The variation in reference curve from memory curve, $\Delta M = M_{ZFC}^{mem} - M_{ZFC}^{ref}$, gives a significant memory dip in 30-80 K as shown in Figure 3.10(c). Hence, detection of the thermal memory effect in ZFC-FC conditions further supports the claim that the system exhibits frustrating magnetic phases.

3.4.5.2 Ageing

The relaxation memory is performed considering ZFC protocol in a negative temperature cycle [41] as shown in Figure 3.11(a). During ZFC condition [94], system is allowed to cool down up to temperature of 30 K in the absence of a magnetic field. At temperature, 30 K, named as t_1, the system is kept for ageing of 5000 seconds in the presence of 50 Oe field following recording of magnetization. The exponential increase in the moment is found with an increase in the ageing period. Further, the temperature is reduced temporarily to 20 K, named as t_2, for 7500 seconds and moments are recorded in the same field. Consequently, temperature is raised again to 30 K and the moment is recorded

for the next 7500 seconds in the same field. It is observed that when the system comes back to its earlier thermal condition, the trend of magnetization follows its earlier relaxation pattern with a continuation as shown in Figure 3.11(b) (coloured area).

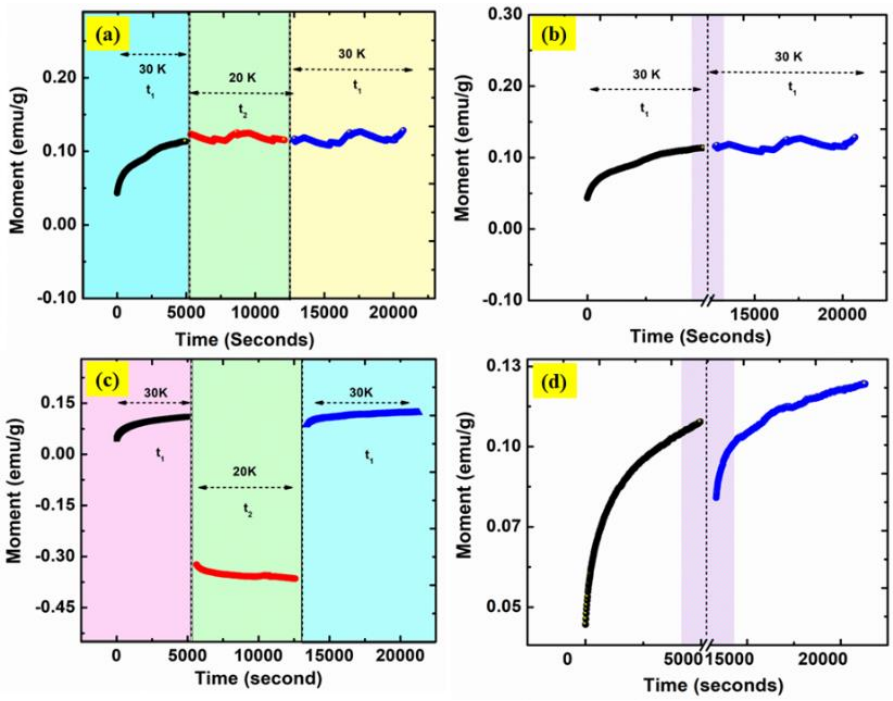

Figure 3.11: (a) Negative T-cycle ZFC ageing, (b) Continuation before and after ageing, (c) Reverse ageing relaxation in ZFC condition and (d) Continuation curve before and after ageing of Ensemble of Two-Dimensional flakes (ETD).

It is because of the thermal memorization of the spins of their age at t_1. For ZFC reverse relaxation ageing measurement, system is further cooled down to 30 K at zero applied field. After reaching 30 K, a field of 50 Oe is employed and the magnetization is recorded for 5000 seconds. After 5000 seconds, the temperature is further cooled to 20 K and applied field is turned off. The moment is recorded for this condition for 7500 seconds. The system is kept for re-warming to 30 K and 50 Oe field is employed to measure the moments the next 8000 seconds. The ZFC reverse relaxation trend is shown in Figure 3.11(c). The continuation trend

is shown in Figure 3.11(d) and a broken symmetry is observed after and before ageing relaxation trend.

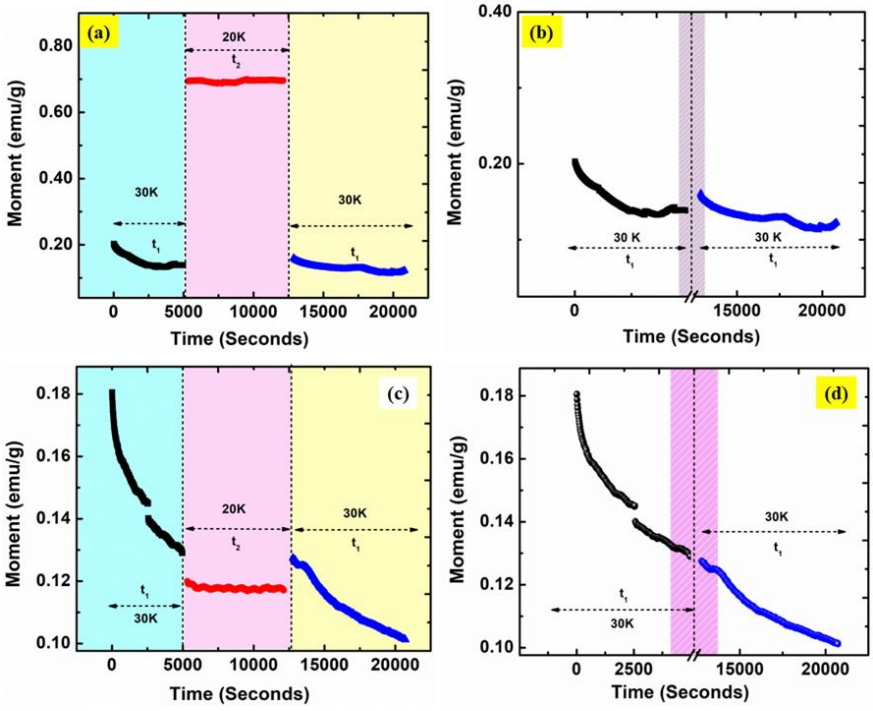

Figure 3.12: (a) Reverse T-cycle FC ageing, (b) Continuation before and after ageing, (c) Negative T-cycle in FC condition, and (d) Continuation before and after ageing of Ensemble of Two-Dimensional (2D) flakes (ETD).

Similarly, for FC reverse relaxation ageing [41], system ETD is cooled down to 30 K in 50 Oe field. After turning off the field, magnetization is recorded for 5000 seconds and marked as t_1. Further, system ETD is cooled down to 20 K. A field of 50 Oe is employed and magnetization is recorded for 7500 seconds. After re-heating to 30 K, field is turned off following recording of magnetization for the next 8000 seconds. The FC reverse relaxation trend is shown in Figure 3.12(a). The continuation of the relaxation trend after and before ageing is imprinted in Figure 3.12(b) for reverse FC relaxation. In the case of Field Cooling (FC) condition, the system is cooled down to 30 K in 50 Oe field. The moment is measured for 5000 seconds after switching the field. A decay in magnetization is observed with an increase in time as shown in Figure 3.12(c). A further cooling

of temperature to 20 K is employed when there is no field and magnetization is calculated for 7500 seconds, which shows a constant value with time. In the end, the system is warmed back to the earlier temperature, 30 K, in absence of field and moment is recorded for a period of the next 7500 seconds, which again shows an exponential trend with time. As shown in Figure 3.12(d), if the intermittent perturbation is removed, it is observed that the continuation at 30 K after a perturbation has not been broken down as observed in the colored marked region.

Hence, though the relaxation trend is revived, no magnetic memory is imprinted in case of the ZFC and FC reverse ageing relaxation process, memory effect is observed in negative T-cycle in both FC-ZFC conditions. In the droplet model of the SG phase, the prior spin configuration is recovered anticipating a symmetric trend of magnetic relaxation about both the reverse and negative T cycle. In a hierarchical model, the prior spin configuration does not exist and is destroyed resulting in an asymmetric behaviour with no memory imprint in moment relaxation. Considering the above norms, observed asymmetric responses in reverse ageing relaxation protocols in both FC and ZFC conditions confirm hierarchical arrangement of metastable states of free energy following the hierarchical model of SG. This behaviour is not attributed to individual spins, but to competing effect of interparticle/intracluster interactions dominated in SG [47, 48].

The various kind of glassy systems is signified by taking into account magnetic relaxation properties. To investigate the glassy characteristics, magnetic relaxation is performed at a temperature of 30 K, much lower than the freezing temperature, considering both FC and ZFC conditions as shown in Figure 3.13(a, b). The system is kept for cooling with/without a magnetic field till the necessary temperature and after a certain waiting period, a 50 Oe field is employed and evolution of the magnetization over time is recorded. The time-dependent magnetization curve is fitted following the standard stretched exponential

function as given in equation 2.16 of Chapter 2. A zero value of β of equation 2.16 signifies the absence of relaxation with constant magnetization over time. In the current scenario, the fitted value of β is calculated as 0.5 for both ZFC and FC conditions. Additionally, as β is less than 1, it denotes that activation occurs against numerous anisotropic barriers as the system progresses following intermediate metastable states [41]. The presence of competing

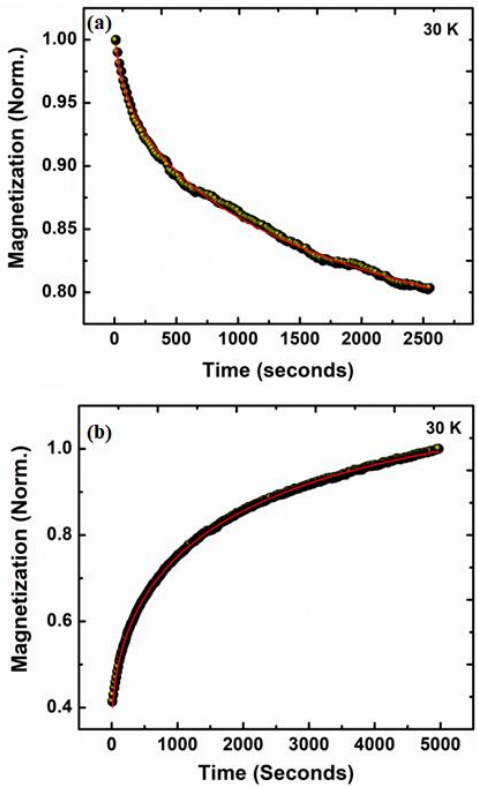

Figure 3.13: Magnetic relaxation with standard stretched exponent fitting at (a) FC condition, (b) ZFC condition of δ-MnO_2@$NiFe_2O_4$ (Ensemble of Two-Dimensional (2D) flakes (ETD)).

ordering among MNPs leads to frustration. A competing trend between positive and negatively aligned moments can be addressed as a reason for SG state evolution in ETD. The dynamic of metastable states with a rugged energy landscape and random magnetic interactions having quantum fluctuations is the reason for such cluster SG freezing. However, a correlated effect of exchange and

dipolar interaction with a lower degree of freedom gives rise to significant MME and ageing effects in the 2D nanosystems.

3.5 CONCLUDING REMARKS

In conclusion, an organized spin dynamics analysis with non-ergodic quantum behaviour is addressed in the ensemble of 2D Manganese dioxide flakes decorated over nickel ferrite MNPs. A broad energy barrier distribution is reflected in the ZFC magnetization trend. A blocking temperature shifting in a low-temperature regime is due to the interacting domain of the system. A quasi-constant trend of FC magnetization curve is the hallmark of interparticle interaction in the secondary structure. The lower temperature region below blocking temperature in FC magnetization condition is showing a lowering of magnetization trend with a further lower in temperature, which is a typical signature of the existence of frustrated magnetic states. A high exchange field is reflected with a high magneto-crystalline anisotropy constant, resulting complex anisotropy energy landscape. The collective spin freezing is imprinted in ensemble from the MME in both FC and ZFC conditions. Dynamic magnetization study gives significant evidence of cluster SG freezing. The achieved spin-glass state evolution is a result of a cluster of spin, rather than atomic level freezing of spins. The progressive freezing of spin is governing the moment relaxation with dynamic scaling behaviour in the domains of 2D nanosystems, with enhanced shape anisotropy and quantum fluctuations, facilitating slow spin dynamics. As a consequence, non-ergodic quantum phenomena with prominent MME and ageing relaxation are achieved with the aid of hierarchical metastable states in the free-energy landscape by considering an ensemble decorated with interacting anisotropic nanosystems. Hence, this chapter illustrates an intriguing magnetic behaviour with an effectual magnetic anisotropy field, magneto-crystalline anisotropy with notable magnetic memory effects and considerable ageing relaxation.

References:

[1] Woińska, M., Szczytko, J., Majhofer, A., Gosk, J., Dziatkowski, K. and Twardowski, A. Magnetic interactions in an ensemble of cubic nanoparticles: A Monte Carlo study. *Physical Review B,* 88:144421, 2013.

[2] Haase, C. and Nowak, U. Role of dipole-dipole interactions for hyperthermia heating of magnetic nanoparticle ensembles. *Physical Review B,* 85:045435, 2012.

[3] Petracic, O. Superparamagnetic nanoparticle ensembles. *Superlattices and Microstructures,* 47:567, 2010.

[4] Muscas, G., Concas, G., Laureti, S., Testa, A. M., Mathieu, R., Toro, J. A., Cannas, C., Musinu, A., Novak, M. A., Sangregorio, C., Lee, S. S. and Peddis, D. The interplay between single particle anisotropy and interparticle interactions in ensembles of magnetic nanoparticles. *Physical Chemistry Chemical Physics*. 20: 28634, 2018.

[5] Bedanta, S. and Kleemann, W. Supermagnetism. *Journal of Physics D: Applied Physics,* 42:013001, 2009.

[6] Balaev, D. A., Semenov, S. V., Dubrovskiy, A. A., Yakushkin, S. S., Kirillov, V. L., Martyanov, O. N. Superparamagnetic blocking of an ensemble of magnetite nanoparticles upon interparticle interactions. *Journal of Magnetism and Magnetic Materials,* 440:199, 2017.

[7] Choi, J., Choi, S., Kucsko, G., Maurer, P. C., Shields, B. J., Sumiya, H., Onoda, S., Isoya, J., Demler, E., Jelezko, F., Yao, N. Y. and Lukin, M. D. Depolarization Dynamics in a Strongly Interacting Solid-State Spin Ensemble. *Physical Review Letters,* 118:093601, 2017.

[8] Denisov, S. I. and Trohidou, K. N. Fluctuation theory of magnetic relaxation for two-dimensional ensembles of dipolar interacting nanoparticles. *Physical Review B,* 64:184433, 2001.

[9] Tackett, R. J., Parsons, J. G., Machado, B. I., Gaytan, S. M., Murr, L. E. and Botez, C. E. Evidence of low-temperature superparamagnetism in Mn3O4 nanoparticle ensembles. *Nanotechnology,* 21:365703, 2010.

[10] Nonextensivity in magnetic nanoparticle ensembles. Ch. Binek, S. Polisetty, Xi He, T. Mukherjee, R. Rajesh, and J. Redepenning, Phys. Rev. B 74, 054432, 2006.

[11] Cowburn, R. P. Property variation with shape in magnetic nanoelements. *Journal of Physics D: Applied Physics,* 33:R1, 2000.

[12] Oyarzún, S., Tamion, A., Tournus, F., Dupuis, V. and Hillenkamp, M. Size effects in the magnetic anisotropy of embedded cobalt nanoparticles: from shape to surface. *Scientific Reports,* 5:14749, 2015.

[13] Hehn, M., Ounadjela, K., Jean-Pierre Bucher, J.-P., Rousseaux, F., Decanini, D., Bartenlian, B., and Chappert, C. Nanoscale Magnetic Domains in Mesoscopic Magnets, *Science,* 272:1782, 1996.

[14] Hu, H., Yuan, Y., Lim, S., Wang., C. H. Phase structure dependence of magnetic behaviour in iron oxide nanorods. *Materials & Design,* 185:108241, 2020.

[15] Baranov, A. N., Panin, G. N., Yoshimura, M., Oh, Y.-J. Growth and magnetic properties of Mn and MnSn-doped ZnO nanorods. *Journal of Electroceramics,* 17: 847, 2005.

[16] Seo, K., Varadwaj, K. S. K., Mohanty, P., Lee, S., Jo, Y., Jung, M.-H., Kim, J. and Kim, B. Magnetic Properties of Single-Crystalline CoSi Nanowires. *Nano Letters,* 7:1240, 2007.

[17] Pastor G. M. and Jensen, P. J. Elementary transitions and magnetic correlations in two-dimensional disordered nanoparticle ensembles. *Physical Review B,* 78:134419, 2008.

[18] Leo, N, Holenstein, S., Schildknecht, D., Sendetskyi, O., Luetkens, H., Derlet, P. M., Scagnoli, V., Lancon, D, Mardegan, R. L., Prokscha, T., Suter, A., Salman,

Z., Lee, S. and Heyderman, L. J. Collective magnetism in an artificial 2D XY spin system. *Nature Communications,* 9: 2850, 2018.

[19] Aslibeiki, B., Kameli, P., Salamati, H., Concas, G., Fernandez, M. S., Talone, A., Muscas, G. and Peddis, D. Co-doped $MnFe_2O_4$ nanoparticles: magnetic anisotropy and interparticle interactions. *Beilstein Journal of Nanotechnology,* 10:856, 2019.

[20] Tamion, A., Raufast, C., Hillenkamp, M., Bonet, E., Jouanguy, J., Canut, B., Bernstein, E., Boisron, O., Wernsdorfer, W. and Dupuis, V. Magnetic anisotropy of embedded Co nanoparticles: Influence of the surrounding matrix. *Physical Review B,* 81:144403, 2010.

[21] Muscas, G., Cobianchi, M., Lascialfari, A., Cannas, C., Musinu, A., Omelyanchik, A., Rodionova, V., Fiorani, D., Mameli, V., Peddis. D. Magnetic Interactions Versus Magnetic Anisotropy in Spinel Ferrite Nanoparticles. *IEEE Magnetic Letters,* 10:1, 2019.

[22] Skubic, B., Hellsvik, J., Nordström, L. and Eriksson, O. A method for atomistic spin dynamics simulations: implementation and examples. *Journal of Physics: Condensed Matter,* 20:315203, 2008.

[23] Hu, T., Mei, X., Wang, Y., Weng, X., Liang, R. and Wei, M. Two-dimensional nanomaterials: fascinating materials in biomedical field. *Science Bulletin,* 64:1707, 2019.

[24] Xiang, B. Ling, D., Lou, H. and Gu, H. 3D hierarchical flower-like nickel ferrite/manganese dioxide toward lead (II) removal from aqueous water. *Journal of hazardous materials,* 325:178, 2017.

[25] Giannozzi, P., Baroni, S., Bonini, N., Calandra, M., Car, R., Cavazzoni, C., Ceresoli, D., Chiarotti, G. L., Cococcioni, M., Dabo, I., Corso, A. D., de Gironcoli, S., Fabris, S., Fratesi, G., Gebauer, R., Gerstmann, U., Gougoussis, C., Kokalj, A.,

Lazzeri, M., Martin-Samos, L., Marzari, N., Mauri, F., Mazzarello, R., Paolini, S., Pasquarello, A., Paulatto, L., Sbraccia, C., Scandolo, S., Sclauzero, G., Seitsonen, A. P., Smogunov, A., Umari, P., and Wentzcovitch, R. M. QUANTUM ESPRESSO: a modular and open-source software project for quantum simulations of materials. *Journal of Physics: Condensed Matter*, 21:395502, 2009.

[26] Rappe, A. M., Rabe, K. M. Kaxiras, E. and Joannopoulos, J. D. Optimized pseudopotentials. *Physical Review B,* 44:13175, 1991.

[27] Perdew J. P. and Zunger, A. Self-interaction correction to density-functional approximations for many-electron systems. *Physical Review B,* 23:5048, 1981.

[28] Nayek, C., Samanta, S., Manna, K., Pokle, A., Nanda, B. R. K., Anil Kumar, P. S. and Murugavel, P. Spin-glass state in nanoparticulate $(La_{0.7}Sr_{0.3}MnO_3)_{1-x}$ $(BaTiO_3)_x$ solid solutions: Experimental and density-functional studies. *Physical Review B,* 93:094401, 2016.

[29] Monkhorst, H. J. and Pack, J. D. Special points for Brillouin-zone integrations. *Physical Review B,* 13, 5188, 1976.

[30] Liu, S., Zhu, Y., Xie, J., Huo, Y., Yang, H. Y., Zhu, T., Cao, G., Zhao, X. and Zhang, S. Direct Growth of Flower-Like δ-MnO_2 on Three-Dimensional Graphene for High-Performance Rechargeable Li-O2 Batteries. *Advanced Energy Materials,* 4: 1301960, 2014.

[31] Zhao, Y., Chang, C., Teng, F., Zhao, Y., Chen, G., Shi, R., Waterhouse, G. I. N., Huang, W. and Zhang, T. Defect-Engineered Ultrathin δ-MnO_2 Nanosheet Arrays as Bifunctional Electrodes for Efficient Overall Water Splitting. *Advanced Energy Materials,* 7: 1700005, 2017.

[32] Feng, S., Yang, W. Zhongbing, W. Synthesis of porous $NiFe_2O_4$ microparticles and its catalytic properties for methane combustion, *Materials Science and Engineering: B,* 176:1509, 2011.

[33] Solís, C., Escolastico, S., Haugsrud, R. and Serra, J. M. Particular Transport Properties of NiFe2O4 Thin Films at High Temperatures. *The Journal of Physical Chemistry C,* 118:24266, 2014.

[34] Kohlbrecher, J. SASfit: A program for fitting simple structural models to small angle scattering data, 2023.

[35] Saikia, K., Kaushik, S.D., Sen, D., Mazumder, S. and Deb. P. Fatty acid as structure directing agent for controlled secondary growth of $CoFe_2O_4$ nanoparticles to achieve mesoscale assemblies: A facile approach for developing hierarchical structures, *Applied Surface Science*, 379:530, 2016.

[36] Perron, H., Mellier, T., Domain, C., Roques, J., Simoni, E., Drot, R. and Catalette, H. Structural investigation and electronic properties of the nickel ferrite NiFe2O4: a periodic density functional theory approach. *Journal of Physics: Condensed Matter,* 19:346219, 2007.

[37] Zuo, X., Yan, S., Barbiellini, B., Harris, V. G. and Vittoria, C. A Computational Study of Nickel Ferrite. *Journal of Magnetism and Magnetic Materials,* 303: e432, 2006.

[38] Yamanaka, M., Uekusa, H., Ohba, S., Saito, Y., Iwata, S., Kato, M., Tokii, T., Muto Y. and Steward, O. W. Correlation of electron density and spin-exchange interaction in dimeric copper(II) formates, acetates and silanecarboxylates. *Acta Crystallographica,* B47:344, 1991.

[39] Devi, E. C. and Soibam, I. Law of Approach to Saturation in Mn–Zn Ferrite Nanoparticles, *Journal of Superconductivity and Novel Magnetism,* 32:1293, 2019.

[40] Yadav, K., Sharma, M., Singh, S., Mukherjee, K. Exotic magnetic behaviour and evidence of cluster glass and Griffiths like phase in Heusler alloys $Fe_{2-x}Mn_xCrAl$ ($0 \leq x \leq 1$). *Scientific Reports,* 9:15888, 2019.

[41] Bag, P., Baral, P. R. and Nath, R. Cluster spin-glass behavior and memory effect in $Cr_{0.5}Fe_{0.5}Ga$, *Physical Review B,* 98:144436, 2018.

[42] Ghanta, S., Das, A., Jana, P., Vrtnik, S., Gačnik, D., Luzar, J., Jelen, A., Koželj, P., Wencka, M., Dolinšek, J. Structure and Spin-Glass Magnetism of the $Mn_xNi_2Zn_{11-x}$ Pseudobinary γ-Brasses at Low Mn Contents. *Inorganic Chemistry,* 60: 12226, 2021.

[43] Chowdhury, M. R., Seehra, M. S., Pramanik, P., Ghosh, S., Sarkar, T., Weise, B. and Thota, S. Antiferromagnetic short-range order and cluster spin-glass state in diluted spinel $ZnTiCoO_4$. *Journal of Physics: Condensed Matter,* 34:275803, 2022.

[44] Bandyopadhyay, M. and Dattagupta, S. Memory in nanomagnetic systems: Superparamagnetism versus spin-glass behavior. *Physical Review B,* 74:214410, 2006.

[45] Sun, Y., Salamon, M. B., Garnier, K. and Averback, R. S. Memory Effects in an Interacting Magnetic Nanoparticle System. *Physical Review Letters*, 91, 167206, 2003.

[46] Sasaki, M., Jonsson, P. E., Takayama, H. and Mamiya, H. Aging and memory effects in superparamagnets and superspin glasses. *Physical Review B*, 71:104405, 2005.

[47] Sibani P. and Hoffmann, K. H. Hierarchical models for aging and relaxation of spin glasses. *Physics Review Letters,* 63:2853, 1989.

[48] Moore, M.A. Bokil, H. and Drossel, B. Evidence for the Droplet Picture of Spin Glasses. *Physics Review Letters,* 81:4252, 1998.

[49] Samarakoon, A., Sato, T. J., Chen, T. Chern, G.-W., Yang, J., Klich, I., Sinclair, R., Zhou, H. and Lee, S.-H. Aging, memory, and nonhierarchical energy landscape of spin jam. *Proceedings of the National Academy of Sciences,* 114: 11806, 2016.